CHEMISTRY

Water- and acid-stable self-passivated dihafnium sulfide electride and its persistent electrocatalytic reaction

Se Hwang Kang[1,2], Joonho Bang[1], Kyungwha Chung[1], Chandani N. Nandadasa[3], Gyeongtak Han[1], Subin Lee[2], Kyu Hyoung Lee[4], Kimoon Lee[5], Yanming Ma[6,7], Sang Ho Oh[1], Seong-Gon Kim[3], Young-Min Kim[1,2], Sung Wng Kim[1,2]*

Electrides have emerged as promising materials with exotic properties, such as extraordinary electron-donating ability. However, the inevitable instability of electrides, which is caused by inherent excess electrons, has hampered their widespread applications. We report that a self-passivated dihafnium sulfide electride ($[Hf_2S]^{2+}\cdot 2e^-$) by double amorphous layers exhibits a strong oxidation resistance in water and acid solutions, enabling a persistent electrocatalytic hydrogen evolution reaction. The naturally formed amorphous Hf_2S layer on the cleaved $[Hf_2S]^{2+}\cdot 2e^-$ surface reacts with oxygen to form an outermost amorphous HfO_2 layer with ~10-nm thickness, passivating the $[Hf_2S]^{2+}\cdot 2e^-$ electride. The excess electrons in the $[Hf_2S]^{2+}\cdot 2e^-$ electride are transferred through the thin HfO_2 passivation layer to water molecules under applied electric fields, demonstrating the first electrocatalytic reaction with excellent long-term sustainability and no degradation in performance. This self-passivation mechanism in reactive conditions can advance the development of stable electrides for energy-efficient applications.

INTRODUCTION

Solid-state materials with excess electrons beyond solvated electrons are always attractive as an efficient electron reservoir that can reduce the energy barrier and improve the efficiency of catalytic reactions and electronic devices (*1*, *2*). However, it is challenging to use their immense reactivity sustainably in active environments, such as in water, analogous to solvated electrons in aqueous solutions having a very short lifetime (*3*, *4*). Electrides are exotic materials with inherent excess electrons acting as anions, which are trapped in structural cavities (*5*–*9*). One beneficial property of electrides is that when their surface is exposed to reactive atmospheres or is activated by an electric field, excess anionic electrons can be directly transferred or emitted into a surface reactant or vacuum with a small barrier, triggering chemical reactions or actuating electronic devices (*10*–*12*). Nevertheless, their chemical instability that originated from excess anionic electrons that are loosely trapped in a large cavity space has been a great obstacle to a persistent and efficient solid-state electron source (*13*). Thus, the development of stable electrides in any active circumstances is the most urgent task.

Ambient-stable electrides are rare and require a particular surface structure that is made from chemically inert materials to passivate the reactive excess electrons. One representative is the room temperature stable $[Ca_{24}Al_{28}O_{64}]^{4+}\cdot 4e^-$ electride that is constructed from three-dimensionally connected subnanometer-sized cages, in which anionic electrons are trapped. At the cleaved surface of the $[Ca_{24}Al_{28}O_{64}]^{4+}\cdot 4e^-$ electride, the subnanometer-sized cages collapse into a chemically inert amorphous structure that is responsible for the stability in an ambient atmosphere and is revealed to have the electride character (*14*, *15*). Recently, other stable electrides have been found in intermetallic compounds, which are constructed from a cage-linked chain structure, but their surface structures need to be investigated (*16*, *17*). In particular, the Y_5Si_3 electride retains its catalytic capability for ammonia synthesis even after being dipped in water (*16*), which implies that the surface structure is most likely chemically inert. However, Y_5Si_3 electrides have not been applied to a catalytic reaction under wet conditions. An electride that is sustainable in reactive conditions such as water and acid and that can simultaneously transfer the excess anionic electrons has not been reported yet. For example, the amorphous layer at the $[Ca_{24}Al_{28}O_{64}]^{4+}\cdot 4e^-$ electride surface is easily soluble in water and alcohols, limiting its use as an electron-donating catalyst in such solutions (*11*). Thus, another approach is required for the development of novel electrides with long-term sustainability in reactive environments, especially in water- and acid-containing conditions. Meanwhile, considering that the performance of applications is exclusively dominated by transferring the excess anionic electrons, the transferred excess anionic electrons need to be compensated for keeping the charge neutrality and preventing the decomposition. For an ideal application, an electrochemical catalyst or electronic device that is sustainably activated by applying electric current is desirable but is not realized yet.

Here, we report a self-passivated electride with double amorphous layers that provides a rational design strategy for permanently sustainable electrides in strongly oxidative water and acid solutions. To demonstrate the availability of chemically stable electride as a catalyst, we also provide the first electrochemical catalytic reaction in water and acid solutions, which makes a breakthrough in the research field of electride materials. In the context of material design, we conceived that the designed electride needs to contain a metallic element, such as Hf, W, or Cr, which tends to form an amorphous oxide as a passivation layer. Several Hf-based binary compounds

[1]Department of Energy Science, Sungkyunkwan University, Suwon 16419, Republic of Korea. [2]Center for Integrated Nanostructure Physics, Institute for Basic Science, Suwon 16419, Republic of Korea. [3]Department of Physics & Astronomy and Center for Computational Sciences, Mississippi State University, Mississippi State, MS 39762, USA. [4]Department of Materials Science and Engineering, Yonsei University, Seoul 03722, Republic of Korea. [5]Department of Physics, Kunsan National University, Kunsan 54150, Republic of Korea. [6]State Key Laboratory of Superhard Materials & Innovation Centre of Computational Physics Method and Software, College of Physics, Jilin University, Changchun 130012, China. [7]International Center of Future Science, Jilin University, Changchun 130012, China.
*Corresponding author. Email: kimsungwng@skku.edu

such as Hf_2S and HfBr have been already synthesized (*18*, *19*) and recently proposed as electride candidates by computational predictions (*20*, *21*). Among the candidates, considering that chalcogens often formulate an amorphous material with transition metals (*22*), we investigated the Hf_2S as a proof-of-concept material.

RESULTS

A two-dimensional electride, dihafnium sulfide

First, we elucidate the detailed electronic state of excess anionic electrons in Hf_2S, which has not been considered in previous calculations (*20*). The calculated crystal structure of Hf_2S in Fig. 1A shows that the excess anionic electrons occupy the two-dimensional interlayer spacing between the cationic layers (fig. S1). This feature is the hallmark of two-dimensional electrides with localized excess anionic electrons. From the density functional theory (DFT) calculations, it is noted that the anionic electrons confined in the vicinity of Hf atoms play a substantial role in the two-dimensional electronic structure. The projected band structure (Fig. 1B) and density of states (DOS) (Fig. 1C) of excess anionic electrons (e^-) near the Fermi level (E_F) show a notable contribution as constituent Hf and S elements, which is analogous to those of carbide electrides (*23*, *24*). The electron localization function (ELF) and charge density map (CDM) on the $(2\bar{1}0)$ plane are shown in Fig. 1 (D and E, respectively). The local maxima of both ELF and CDM can be observed at the crystallographic positions of anionic electrons, indicating that there exist non-nuclear attractors (*25*). Each anionic electron has an atomic charge of $1.3e^-$, which is determined by the integration of charge density within Bader's basin (fig. S1), and forms a dumbbell shape with heads at the center of the Hf triangles of each two-dimensional array at the interlayer space (Fig. 1D and fig. S1). The partial CDM (PCDM) shows that the Hf_2S has a two-dimensional conduction pathway through excess anionic electrons and Hf atoms (Fig. 1F and fig. S1). Moreover, the calculated Fermi surface has a prominent cylindrical shape of a typical two-dimensional electronic system (Fig. 1F). Therefore, all results obtained by DFT calculations strongly suggest that the Hf_2S is a two-dimensional electride with strong localization of excess electrons in a dumbbell shape at interlayer space, which is distinct from the localized excess electrons of two-dimensional $[Ca_2N]^+ \cdot e^-$ and $[Y_2C]^{2+} \cdot 2e^-$ electrides (*9*, *24*).

The two-dimensional layered structure of Hf_2S, which is an anti-TaS_2–type crystal structure that belongs to the $P6_3/mmc$ space group, was confirmed by single-crystal analysis (Fig. 2A), Rietveld refinement of the corresponding powder x-ray diffraction (XRD) pattern (Fig. 2B), and atomic-scale scanning transmission electron microscopy (STEM) observation combined with energy-dispersive x-ray spectroscopy (EDX) mapping (Fig. 2C and fig. S2). The layer unit consists of edge-sharing Hf_6S trigonal prisms in the $[Hf_2S]^{2+}$ layer

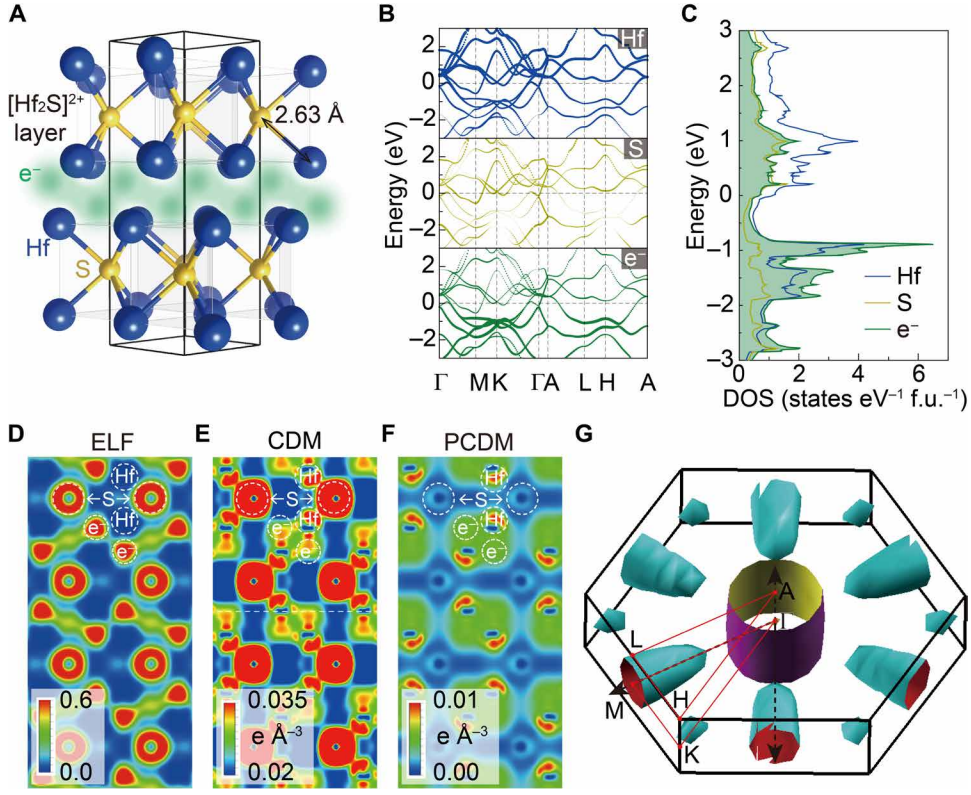

Fig. 1. Two-dimensional layered structure and electronic structure of Hf_2S. (**A**) Calculated crystal structure with a hexagonal unit cell ($a = b = 3.38$ Å, $c = 11.85$ Å, $\alpha = \beta = 90°$, $\gamma = 120°$) represented by solid black lines. Dumbbell-shaped excess anionic electrons (e^-) are localized between $[Hf_2S]^{2+}$ layers. Maxima of excess anionic electrons are located at the Wyckoff position (0.333, 0.667, 0.57), which indicates strong localization at the position of e^-. (**B**) Total and projected band structures. Identical band dispersions imply the strong hybridization state of Hf and excess anionic electron. (**C**) Total and projected DOS per unit energy per formula unit (f.u.) on spheres located at Hf, S, and e^- positions. The DOS of e^- is filled green. (**D**) ELF, (**E**) CDM, and (**F**) PCDM on the $(2\bar{1}0)$ plane. Positions of Hf, S, and e^- are denoted by white dashed circles. (**G**) Fermi surface in the first Brillouin zone.

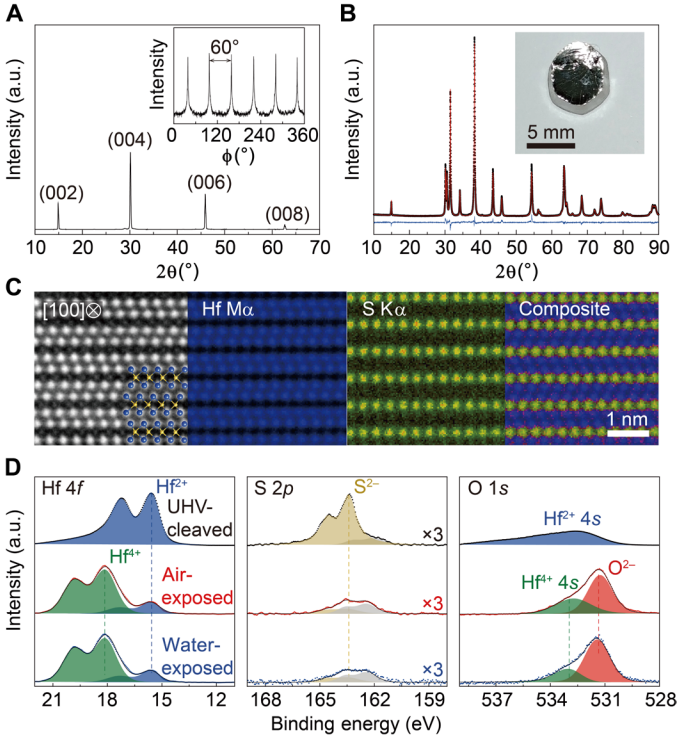

Fig. 2. Characterizations of crystal structure and chemical states for $[Hf_2S]^{2+}\cdot 2e^-$ electride. (**A**) XRD patterns for $[Hf_2S]^{2+}\cdot 2e^-$ single crystal. Out-of-plane 2θ scan (main) and in-plane ϕ scan (inset) for cleaved surface showing well-constructed hexagonal structure with exclusive (00*l*) diffraction and sixfold symmetry, respectively. (**B**) Rietveld refinement of powder XRD pattern. Inset shows a photograph of a cleaved shiny surface. Detailed crystal information from Rietveld refinement listed in table S1. (**C**) Atomic-scale high-angle annular dark-field STEM image and EDX elemental mapping result for the $(2\bar{1}0)$ plane. The calculated structure is superimposed on the observed image and shows good agreement. (**D**) XPS spectra for Hf 4*f*, S 2*p*, and O 1*s* with UHV-cleaved, air-exposed, and water-exposed single crystals. All spectra are measured at the (00*l*) plane and calibrated from the spectrum of reference Au metal (fig. S3). Typical Hf^{4+}, S^{2-}, and O^{2-} spectra are filled green, yellow, and red, respectively. The blue spectrum is expected to be Hf^{2+} because the peak of Hf $4f_{7/2}$ (15.5 eV) is located between the Hf metal (14.0 eV, 0 valence state) and HfO_2 (17.9 eV, 4+ valence state). a.u., arbitrary units.

with a bonding length of 2.63 Å between Hf and S, which is larger than the sum (2.42 Å) of the ionic radii of Hf^{4+} (0.58 Å) and S^{2-} (1.84 Å) (*26*). This discrepancy indicates that the Hf ion has a lower valence state than 4+. To ensure that the valence charges on Hf and S are close to 2+ and 2−, respectively, which were revealed by the Bader's charge analysis on the charge density, we determined the chemical valence states of each element by x-ray photoemission spectroscopy (XPS). As shown in Fig. 2D, from the spectra of the single crystal after cleaving in an ultrahigh vacuum chamber (UHV-cleaved, top), the valence states of Hf and S were determined to be 2+ and 2−, respectively. Furthermore, we conducted a quantitative analysis with core level spectra to confirm the chemical composition, giving a good agreement with a Hf/S nominal atomic ratio of 2 (table S2). These results validate that the Hf_2S is a two-dimensional electride with the chemical formula $[Hf^{2+}{}_2S^{2-}]^{2+}\cdot 2e^-$ with two excess anionic electrons per formula unit, which is consistent with the theoretical calculations. It should be noted that the chemical composition and ratio of components were preserved at the surface of the UHV-cleaved sample. However, for single crystals exposed to air (air-exposed) and water (water-exposed), we found the mixed-valence state of Hf, which is composed of major 4+ and minor 2+ states (Fig. 2D, middle and bottom). From the appearance of the O 1*s* peak in both air- and water-exposed samples, we verified that the Hf^{4+} state is attributed to the formation of hafnium dioxide at the surfaces.

Chemically stable two-dimensional electride, $[Hf_2S]^{2+}\cdot 2e^-$

The surface modification is a key ingredient for stabilizing the two-dimensional $[Hf_2S]^{2+}\cdot 2e^-$ electride. In contrast to previously reported two-dimensional electrides, including $[Ca_2N]^+\cdot e^-$ and $[Y_2C]^{2+}\cdot 2e^-$, which are extremely unstable in air due to the layered open structure that makes excess anionic electrons react with oxygen and water molecules within several minutes (*24*, *27*), the $[Hf_2S]^{2+}\cdot 2e^-$ electride is extraordinarily stable in reactive atmospheres. Both air- and water-exposed powders exhibited no distinct change in the crystal structure, exhibiting identical XRD patterns to that of the pulverized powders of the UHV-cleaved sample (Fig. 3A). Further, the chemical stability in acid solutions was also confirmed (fig. S4). Most of all, it is notable that the two-dimensional layered structure remains unchanged even after soaking in water for 2 months and in acid for 1 month (fig. S4). Besides the crystal structure, the electrical properties also remain unaffected. Figure 3B shows the temperature dependence of the electrical resistivity (ρ) for $[Hf_2S]^{2+}\cdot 2e^-$ electrides that were exposed to different atmospheres, showing that metallic conduction is maintained with only a slight change in resistivity value, which arises from surface oxidation. As shown in the inset of Fig. 3B, both carrier concentration (N_H) and electrical mobility (μ) also showed negligible changes. However, unlike the electrical transport properties, the surface state of the UHV-cleaved sample changed remarkably after exposure to air and water (Figs. 2D and 3C). From the ultraviolet photoemission spectroscopy (UPS) that reveals the work function (WF) values for each sample, it is observed that the metallic Fermi edge (indicated by the red arrow in the inset of Fig. 3C) of the UHV-cleaved sample with a WF value of 3.6 eV disappeared and the insulating states with an increased WF value of ~4.5 eV evolved upon exposure to air and water. Thus, we speculate that the entire surface is covered by insulating hafnium dioxide with a measured WF value of ~4.5 eV, which is slightly smaller than the reported value (*28*), most likely due to the contribution from the transferred excess anionic electrons, passivating the $[Hf_2S]^{2+}\cdot 2e^-$ electride and rendering the extraordinary chemical stability. To elucidate the surface modification in detail, we observed the surface structure by using TEM combined with EDX elemental mapping.

Double amorphous passivation layer-driven chemical stability under oxidizing condition

Figure 3D shows high-resolution TEM (HRTEM) images for samples prepared in three different atmospheres. In the UHV-cleaved sample, an amorphous layer (greenish region) was visible on the surface of crystalline $[Hf_2S]^{2+}\cdot 2e^-$ electride (Fig. 3D and fig. S5). A noticeable change is that the amorphous layer was expanded in thickness and divided into two different amorphous layers in the air- and water-exposed samples, forming a double-layered surface structure. From the EDX elemental mapping results for the water-exposed sample (Fig. 3, E and F), the inner (yellowish region) and outermost (reddish region) amorphous layers are revealed as Hf–S and Hf–O amorphous compounds, respectively. Considering together with the composition ratio obtained from XPS measurements (table S2),

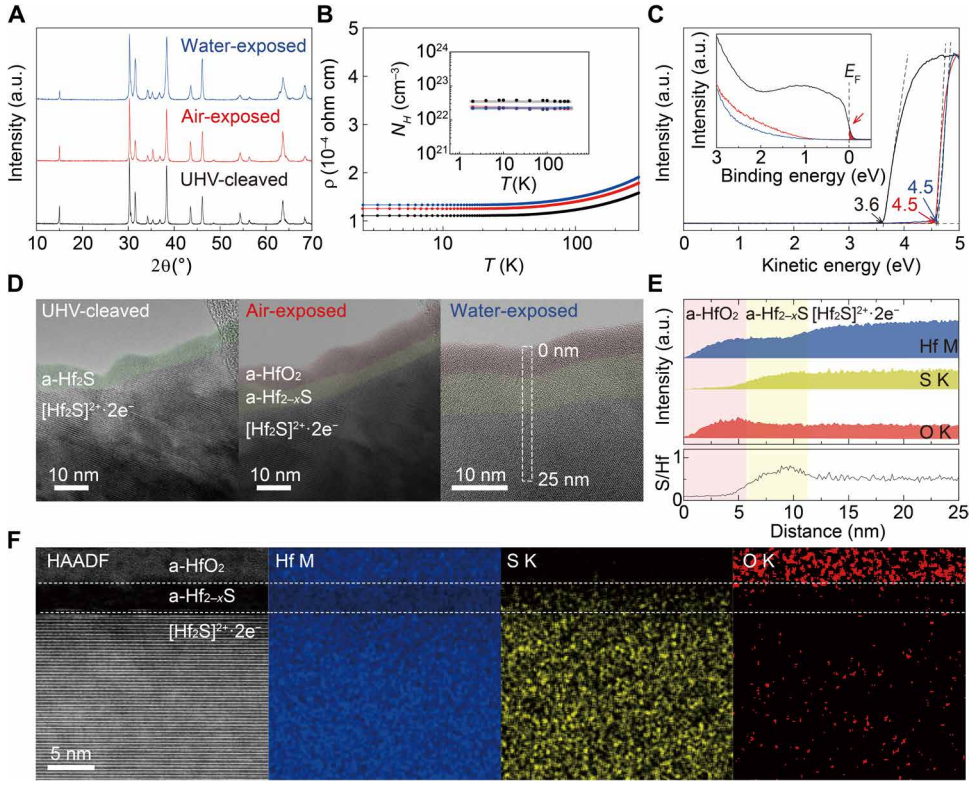

Fig. 3. Water-durable $[Hf_2S]^{2+}\cdot 2e^-$ electride passivated by double amorphous layers. Comparison of (**A**) powder XRD patterns, (**B**) electrical transport properties, and (**C**) UPS spectra for UHV-cleaved (black), air-exposed (red), and water-exposed (blue) samples (Materials and Methods). XRD and UPS results indicate the increased resistivity of air- and water-exposed samples attributed to increased contact resistance between the electrode and insulating a-HfO_2 at the $[Hf_2S]^{2+}\cdot 2e^-$ electride surface. Carrier concentration (N_H) of 3.04×10^{22} cm^{-3} agrees well with the calculated value of 3.44×10^{22} cm^{-3} based on two electrons per formula unit with a chemical formula of $[Hf_2S]^{2+}\cdot 2e^-$. Inset of (C) shows the metallic Fermi edge of the UHV-cleaved sample. (**D**) HRTEM images of surface structures for UHV-cleaved, air-exposed, and water-exposed $[Hf_2S]^{2+}\cdot 2e^-$ electrides. (**E**) STEM-EDX elemental mapping profile in the region of the white dashed box in (D). S- and O-dominant amorphous layers highlighted with different colors are distinguishable by a contrast difference (fig. S6). Oxygen signal underneath a-HfO_2 layer ascribed to oxidation of top and bottom surface [perpendicular direction to the images in (D)] of the TEM sample. (**F**) STEM-EDX elemental-mapping images for the water-exposed $[Hf_2S]^{2+}\cdot 2e^-$ electride.

it is certain that the amorphous layer of the UHV-cleaved sample is amorphous dihafnium sulfide (a-Hf_2S), and the outermost amorphous layer of the air- and water-exposed samples is amorphous hafnium dioxide (a-HfO_2). This result thus concludes that the WF values of 3.6 and 4.5 eV (Fig. 3C) originate from the a-Hf_2S and a-HfO_2, respectively. Furthermore, it implies that the metallic a-Hf_2S layer with a low WF value of 3.6 eV is unstable in air and water atmospheres, reacting with oxygen and forming a chemically stable a-HfO_2 layer. This intriguing surface modification suggests that the a-Hf_2S probably contains excess anionic electrons, maintaining the electride character, analogous to the amorphous $[Ca_{24}Al_{28}O_{64}]^{4+}\cdot 4e^-$ electride (*14*, *15*). From the compositional distributions of double amorphous layers obtained by EDX elemental mapping [Fig. 3, E and F, see also electron energy-loss spectroscopy (EELS) results in fig. S5], it is verified that the Hf ions of the a-Hf_2S layer undergo an outward diffusion to form the a-HfO_2, resulting in a Hf-deficient a-$Hf_{2-x}S$ layer. Compared with the intensities of Hf and S for crystalline $[Hf_2S]^{2+}\cdot 2e^-$, an increase in S/Hf ratio in the a-$Hf_{2-x}S$ layer is observed (the yellowish region in Fig. 3E). Once the a-Hf_2S is exposed to air or water, the excess anionic electrons in a-Hf_2S are transferred to the adsorbed oxygen molecules at the surface and bind with outward diffused Hf ions to form a-HfO_2, leading to an a-HfO_2/a-$Hf_{2-x}S$/$[Hf_2S]^{2+}\cdot 2e^-$ structure denoted as a self-passivated $[Hf_2S]^{2+}\cdot 2e^-$ electride. When ~ 5 to 10 nm, further oxidation is prevented via blocking ion diffusion and electron transfer by a-HfO2, a well-known chemically inert compound even in some strong acids (*29*). Moreover, real-time TEM experiments with in situ heating show no significant changes in phases up to ~700°C, which shows that the thermal stability of the self-passivated $[Hf_2S]^{2+}\cdot 2e^-$ electride is also excellent (fig. S6 and movie S1). It should be noted that clarifying the unprecedented self-passivation mechanism by a double amorphous layer structure supports our material design strategy, the selection rule of constituent elements for the formation of amorphous oxide as a passivation layer, triggering the development of chemically stable electrides and exploring the surface structure, even for the existing stable electrides.

The first electrocatalytic reaction of electrides in acid solutions

Last, given the permanent stability of the self-passivated $[Hf_2S]^{2+}\cdot 2e^-$ electride under strongly oxidizing conditions, an electrocatalytic hydrogen evolution reaction (HER) was performed in a 0.5 M sulfuric acid solution (movie S2). Figure 4 (A and B) shows the HER polarization curves from linear-sweep voltammetry and Tafel plots for the self-passivated $[Hf_2S]^{2+}\cdot 2e^-$ electride, a-HfO_2 thin films with different thickness (fig. S7), and HfO_2 powder. To clarify the role of

the excess electrons of the $[Hf_2S]^{2+}\cdot 2e^-$ electride on HER, a 10-nm-thick a-HfO_2 thin film, which has a similar thickness and chemical states to the a-HfO_2 layer on the $[Hf_2S]^{2+}\cdot 2e^-$ electride, was prepared on the gold electrode (fig. S7). Both the a-HfO_2 thin film with 100-nm thickness and HfO_2 powders showed no HER activity (Fig. 4A and fig. S7). For the a-HfO_2 thin film with 10-nm thickness, the performance was also poor, displaying an overpotential to achieve the current density of 10 mA cm^{-2} and Tafel slope of 581 mV and 141 mV $decade^{-1}$, respectively. It is noticeable that the self-passivated $[Hf_2S]^{2+}\cdot 2e^-$ electride exhibits a nearly identical Tafel slope value of 130 mV $decade^{-1}$, suggesting that the dominant chemical reaction on the surface is unchanged; however, its electrocatalytic activity for HER is largely enhanced to an overpotential of 355 mV to reach 10 mA cm^{-2}. From the performance difference between the 10-nm-thick a-HfO_2 thin film and the self-passivated $[Hf_2S]^{2+}\cdot 2e^-$ electride, it is clear that the excess anionic electrons of the $[Hf_2S]^{2+}\cdot 2e^-$ electride have a critical role in the electrocatalytic HER. Based on the theoretical calculations and experimental results (Fig. 3C and fig. S8), the WF values of the $[Hf_2S]^{2+}\cdot 2e^-$ electride and a-Hf_2S electride are of ~3.04 and 3.6 eV, respectively. These low WF values result in lower energy barrier (E_b) at the junction with a-HfO_2 than that of Au/a-HfO_2, as shown in Fig. 4C.

These results are remarkable from the fact that the self-passivated $[Hf_2S]^{2+}\cdot 2e^-$ electride does not react with water and acid solution, in contrast to the previous unstable electrides that are easily decomposed in water (fig. S4), but shows the electrocatalytic reaction under the applied electric field. In other words, the excess electrons of the self-passivated $[Hf_2S]^{2+}\cdot 2e^-$ electride were transferred through the thin a-HfO_2 passivation layer under the applied electric field, facilitating the persistent electrocatalytic HER. However, the moderate HER performance of the self-passivated $[Hf_2S]^{2+}\cdot 2e^-$ electride, which is lower than that of state-of-the-art materials such as defect-rich ultrathin two-dimensional MoS_2 (*30*), further requires the defect engineering and surface structure modification to enhance the active sites. The modification of passivated surface structure, such as metal nanoparticle loading, improves the electrocatalytic performances of the self-passivated $[Hf_2S]^{2+}\cdot 2e^-$ electride (fig. S7). On the basis of the above results, possible mechanisms for the electrocatalytic HER over the self-passivated $[Hf_2S]^{2+}\cdot 2e^-$ electride are summarized in Fig. 5. The three generally postulated mechanisms in the HER are the Volmer (forming adsorbed hydrogen atoms, H_{ads}, originated in the reaction between proton, H^+, and electron), the Heyrovsky (reaction of H^+, H_{ads}, and electron), and the Tafel (recombination of H_{ads}) (*31*). Given the value of the Tafel slope for the self-passivated $[Hf_2S]^{2+}\cdot 2e^-$ electride, it is suggested that the Volmer step is the rate-determining step. The present HER performance and the crystal structure of the self-passivated $[Hf_2S]^{2+}\cdot 2e^-$ electride catalyst were persistently maintained over 1 week (5000 cycles; figs. S4 and S7), demonstrating that a sustainable electride catalyst even in strong acid-containing solutions is successfully developed.

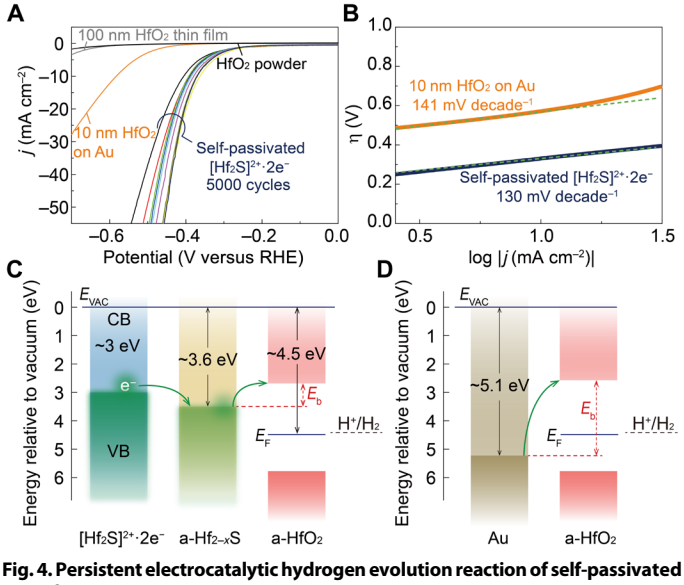

Fig. 4. Persistent electrocatalytic hydrogen evolution reaction of self-passivated $[Hf_2S]^{2+}\cdot 2e^-$ electride in acid solution. (**A**) Polarization curves and (**B**) Tafel plots for self-passivated $[Hf_2S]^{2+}\cdot 2e^-$ electride, HfO_2 powder, and thin films. The thick HfO_2 powder (~45 μm) and film (~100 nm) are nonactive, whereas thin enough HfO_2 film (~10 nm) shows HER activity with poor performance due to the tunneling current. HER performances of the self-passivated $[Hf_2S]^{2+}\cdot 2e^-$ electride maintained over 1 week (5000 cycles). The 5000th cycle of polarization curves selected to plot the Tafel slope (fig. S7). Plausible band diagrams of (**C**) self-passivated $[Hf_2S]^{2+}\cdot 2e^-$ electride and (**D**) HfO_2 thin film on Au for electron transfer to evolve the hydrogen gas. The WF values are acquired from DFT calculations (for the $[Hf_2S]^{2+}\cdot 2e^-$ electride), UPS experiments (for the a-$Hf_{2-x}S$ and a-HfO_2), and literature (*37*) for Au.

DISCUSSION

In summary, the development of the self-passivated $[Hf_2S]^{2+}\cdot 2e^-$ electride with persistent electrocatalytic characteristics presents a promising opportunity as a sustainable electride catalyst under reactive atmospheric conditions. From the successful demonstration of outstanding chemical stability originated from the double amorphous layer structure, which is the key factor of self-passivation mechanism in the Hf-based electride, the design strategy for a stable electride is readily extendable to multinary compounds composed of ubiquitous elements that have a functional passivation layer, allowing one to tune the surface properties. In addition to the unprecedented electrochemical catalytic reactions, we anticipate that our work will

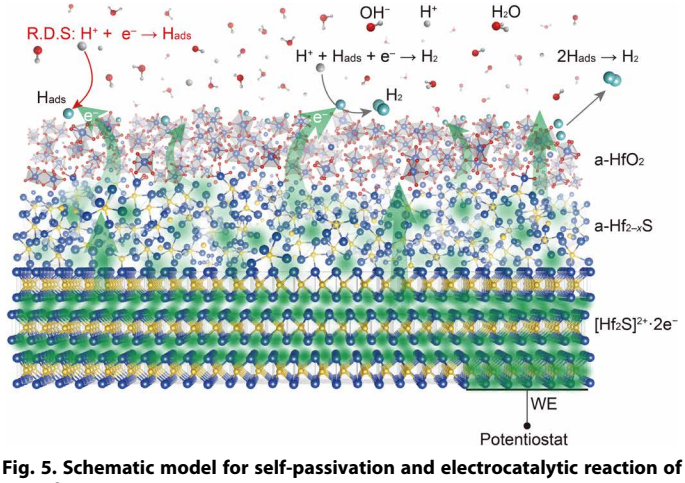

Fig. 5. Schematic model for self-passivation and electrocatalytic reaction of $[Hf_2S]^{2+}\cdot 2e^-$ electride. Structural model and possible pathway for HER over the self-passivated $[Hf_2S]^{2+}\cdot 2e^-$ electride as a working electrode. Volmer ($H^+ + e^- \rightarrow H_{ads}$, ion discharge with the formation of adsorbed hydrogen, H_{ads}), Heyrovsky ($H^+ + e^- + H_{ads} \rightarrow H_2$, subsequent desorption of H_{ads}), and Tafel ($2H_{ads} \rightarrow H_2$, recombination of H_{ads}) reactions occur at the surface of a-HfO_2 with transferring excess electrons from electride.

stimulate further research for exploiting electronic devices with long-term stability in self-passivated electrides.

MATERIALS AND METHODS

Sample preparation

All synthetic steps were carried out in glove boxes filled with high-purity argon gas (Ar 99.999%) to minimize the oxidation of raw materials and synthesized samples. Stoichiometric polycrystalline $[Hf_2S]^{2+}\cdot 2e^-$ electrides were synthesized by the arc melting method under high-purity Ar atmosphere. We mixed and ground Hf powder (Alfa Aesar; 99.6%) and S trace metal basis (Sigma-Aldrich; 99.998%) in a 2:1 molar ratio. To minimize the vaporization of S via the arc melting method, mixed powder was pelletized and sintered at 500°C for 5 days in vacuum-sealed quartz tubes (a few millitorr) and then the quartz tubes were water-quenched down to room temperature, so that sintered pellets could be the mixture of several Hf-S intermediate compounds, such as HfS_2, HfS, HfS_3, and Hf_2S. These intermediate compounds were melted in the Ar-filled arc melting chamber over 2000°C to fabricate polycrystalline coin- and rod-shaped $[Hf_2S]^{2+}\cdot 2e^-$ electride samples. To obtain a single phase and ensure the homogeneity of the samples, we repeated the melting process at least three times. Coin-shaped polycrystals were used to make powder for structural characterization and fabricate working electrodes for electrochemical experiments. Single-crystalline $[Hf_2S]^{2+}\cdot 2e^-$ electrides were grown by the floating zone melting method using polycrystalline rod-shaped $[Hf_2S]^{2+}\cdot 2e^-$ electrides and pieces of seed. Around 3 atm of pressure was applied into the chamber with high-purity Ar gas to prevent vaporization of S during the process. The growing speed was 1 to 3 mm/hour, and the rotation speed of feed and seed rods were 4 to 10 rpm because of the low-melt viscosity of the $[Hf_2S]^{2+}\cdot 2e^-$ electride.

Amorphous HfO_2 thin films are prepared by the pulsed laser deposition method at room temperature. Using pure hafnium metal target, Hf films were deposited on a Cr/Au-coated SiO_2 substrate under an Ar pressure of 10^{-6} torr by using KrF excimer laser ($\lambda = 248$ nm) with a fluence of 6.5 to 7.0 J cm^{-2} and a reputation rate of 5 Hz. Then, the Hf films were exposed to air to form a-HfO_2, similar to the formation of an a-HfO_2 layer on the $[Hf_2S]^{2+}\cdot 2e^-$ electride. The commercial HfO_2 powders (Alfa Aesar; 99.95%, 325 mesh powder) were also used for the HER experiments.

Structural characterization by XRD

The crystal structure of Hf_2S was investigated by XRD using a Rigaku SmartLab diffractometer with monochromatic Cu Kα radiation (8.04 keV) at room temperature. The well-ground powder samples and single crystals were prepared in glove boxes and measured in a plastic dome-type stage filled with Ar gas to avoid oxidation during measurements. Rietveld refinements of the powder XRD data were conducted with the GSAS-II software. To confirm the effect of oxidation to the crystal structure of the $[Hf_2S]^{2+}\cdot 2e^-$ electride, we prepared unoxidized powder handled in Ar-filled glove boxes and oxidized powder neglected in the air and water over 2 months. Then, the same XRD measurement procedures were conducted for each sample. The UHV-cleaved sample in Fig. 3A was prepared in glove boxes filled with high-purity Ar gas by cutting and pulverizing to make fresh surfaces.

DFT calculations

DFT calculations were performed using the generalized gradient approximation with the Perdew-Burke-Ernzerhof functional and the projector augmented plane-wave method implemented in the Vienna ab initio simulator program (VASP) code (*32*–*34*). We used a unit cell that contains two formula units of Hf_2S (see Fig. 1A and fig. S1). The wave function of electrons was expanded in a plane-wave basis set with a cutoff energy of 500 eV. Reciprocal space was sampled with a $17 \times 17 \times 4$ Monkhorst-Pack *k*-point mesh for ELF (*35*), charge density, and partial charge density calculations. We performed geometric optimizations to relax the positions of ions and cell shape until the energy change between two successive ionic/cell relaxation steps was less than 10^{-5} eV. An empty sphere with a Wigner-Seitz radius of 1.207 Å was used to obtain the projected band structure and DOS on the position of the excess electron ("e^-" site). The local (atomic) charge of each ion including the excess anionic electron was computed by Bader's charge decomposition method (*36*). The Bader volume for each site is computed as the volume containing a single charge density maximum and is separated from other volumes by a zero-flux surface of the gradients of the charge density.

Photoemission spectroscopy measurements and characterization

XPS and UPS measurements were performed to investigate chemical and electronic states of $[Hf_2S]^{2+}\cdot 2e^-$ electride surface. To obtain the O- and C-free fresh surface of $[Hf_2S]^{2+}\cdot 2e^-$ electrides, we cleaved the (00*l*) plane of the single-crystalline $[Hf_2S]^{2+}\cdot 2e^-$ electride (referred to as UHV-cleaved sample) under ultrahigh vacuum (UHV) conditions (~10^{-10} torr) with a post attached with Torr Seal before photoemission spectroscopy measurements. For oxidized samples (air- and water-exposed), the surface was cleaned up with 300°C heating in the chamber maintaining UHV condition to reduce the contamination of hydrocarbon, which is easily adsorbed to the sample surface under ambient atmosphere. Then, the measurement was carried out under a vacuum of ca. 3×10^{-10} torr. The photoemission results were obtained using a Scienta R4000 electron analyzer with an Al Kα x-ray source (1486.7 eV) and a discharge lamp that emitted an excitation line of He Iα (21.2 eV). Core spectra of Hf 4*s* and 4*f*, S 2*p*, and O 1*s* were measured for analysis, and all spectra were fitted by comparing the binding energies of the component peaks. Because the cleaved surface of the $[Hf_2S]^{2+}\cdot 2e^-$ electride is metallic, the Hf component peak was fitted with an asymmetric line shape, which arises from final-state effects. Every peak was calibrated by the spectrum of hydrocarbon on the sample and reference Au attached next to the sample. In the WF measurement with UPS, the negative bias voltage of 15 V was applied to clarify that the vacuum level of the sample exceeds that of an electron analyzer.

Electrical transport measurements and characterization

The resistivities and Hall effect measurements were performed to confirm the oxidation effects on the electrical properties. Three different samples, which are cleaved in the glove boxes (UHV-cleaved), exposed to air for 1 month (air-exposed), and immersed in the water for 1 month (water-exposed), were prepared and Au was deposited as electrodes with a thermal evaporator equipped in a glove box onto the surface of the samples to eliminate the noise from contact resistance with four-point and Hall bar configurations. After the contacts were made, Apiezon N grease was coated onto the sample surfaces to prevent further oxidation during measurements. The temperature-dependent resistivities and Hall effect measurements were performed by the physical property measurement system (PPMS DynaCool, Quantum

Design). The carrier concentrations (N_H) were derived from the Hall coefficient (R_H) with the assumption that the electron mobility is much higher than the hole mobility. The equation of the Hall coefficient is given by

$$R_H = \frac{N_h\mu_h^2 - N_e\mu_e^2}{e(N_h\mu_h + N_e\mu_e)^2}$$

Here, N_e is the electron density, N_h is the hole concentration, μ_e is the electron mobility, μ_h is the hole mobility, and e is the elementary charge. Moreover, the Hall coefficient may become a simple formula, $|R_H| = 1/N_e$ with the assumption above. The carrier concentration and mobility (μ) of the $[Hf_2S]^{2+}\cdot 2e^-$ electride in the inset of Fig. 3B is deduced from this simple formula. The UHV-cleaved sample in Fig. 3B was prepared in glove boxes filled with high-purity Ar gas by cutting and cleaving to make fresh surfaces.

TEM observation

TEM experiments were performed using a double-corrected TEM (JEM-ARM200F, JEOL) equipped with a cold field emission source, operating at 200 kV. To prevent oxidation of the TEM sample, a single-tilt vacuum transfer holder (Model VTST-4006, Gatan) was used for TEM experiments (UHV-cleaved samples). TEM samples for HRTEM and EELS were prepared as powder cleaved from a single crystal in the high-purity Ar-filled glove boxes. Dual-beam focused ion beam (AURIGA CrossBeam Workstation, Carl Zeiss) was also used to obtain atomic-scale STEM images and chemical EDX mapping data with JEOL-EDX in the STEM imaging mode. Dual-EDX detector was used to acquire atomic-scale EDX mapping data of the sample, and each detector has an effective detection area of 100 mm^2. The sample drift during the acquisition was compensated by tracking the reference atom position assigned at the beginning of the acquisition. EELS experiments were performed using the same microscope equipped with a GIF system (Model 965 GIF Quantum ER). The spectrometer was set to an energy dispersion of 0.2 eV $channel^{-1}$, and the energy resolution at the zero-loss peak is 0.9 eV.

In situ TEM heating experiments were conducted using a double-corrected TEM (JEM-ARM300F, JEOL) operated at 300 kV with Si micro-electromechanical systems–based in situ TEM heating holder (Wildfire, DENSsolutions). The specimen for the heating experiment was prepared by Focused Ion Beam (FIB) lift-out (Helios NanoLab 450 F1, FEI). The temperature was increased to 900°C in 100°C with a ramping rate of 1°C/s after stabilization for ~5 min at each temperature. TEM images were recorded with a complementary metal-oxide semiconductor camera with 4k resolution (OneView, Gatan).

Electrochemical characterization

The electrochemical testing took place in a three-electrode configuration. A graphite rod was used as a counter electrode to avoid Pt contamination effects, Ag/AgCl was used as a reference electrode, and the bulk self-passivated $[Hf_2S]^{2+}\cdot 2e^-$ electride disks (4 mm by 4 mm by 0.1 mm) were used as a working electrode. All tests were investigated in 50 ml of 0.5 M sulfuric acid (H_2SO_4) electrolyte. The applied potential was 0.05 to −1.0 V and the sweep rate was 5 mV/s. All conducting parts except for the reacting surface were covered with transparent nail polish. Commercial HfO_2 powders with glassy carbon electrode and 10- and 100-nm-thick HfO_2 film were also tested as a working electrode to compare HER activities with the self-passivated $[Hf_2S]^{2+}\cdot 2e^-$ electride.

SUPPLEMENTARY MATERIALS

Supplementary material for this article is available at http://advances.sciencemag.org/cgi/content/full/6/23/eaba7416/DC1

REFERENCES AND NOTES

1. D. Zhu, L. Zhang, R. E. Ruther, R. J. Hamers, Photo-illuminated diamond as a solid-state source of solvated electrons in water for nitrogen reduction. *Nat. Mater.* **12**, 836–841 (2013).
2. K.-B. Kim, M. Kikuchi, M. Miyakawa, H. Yanagi, T. Kamiya, M. Hirano, H. Hosono, Photoelectron spectroscopic study of C12A7:e^- and Alq_3 interface: The formation of a low electron-injection barrier. *J. Phys. Chem. C* **111**, 8403–8406 (2007).
3. A. Migus, Y. Gauduel, J. L. Martin, A. Antonetti, Excess electrons in liquid water: First evidence of a prehydrated state with femtosecond lifetime. *Phys. Rev. Lett.* **58**, 1559–1562 (1987).
4. J. Zhao, B. Li, K. Onda, M. Feng, H. Petek, Solvated electrons on metal oxide surfaces. *Chem. Rev.* **106**, 4402–4427 (2006).
5. J. L. Dye, Electrides: Early examples of quantum confinement. *Acc. Chem. Res.* **42**, 1564–1572 (2009).
6. J. L. Dye, Electrides: Ionic salts with electrons as the anions. *Science* **247**, 663–668 (1990).
7. S. Matsuishi, Y. Toda, M. Miyakawa, K. Hayashi, T. Kamiya, M. Hirano, I. Tanaka, H. Hosono, High-density electron anions in a nanoporous single crystal: $[Ca_{24}Al_{28}O_{64}]^{4+}(4e^-)$. *Science* **301**, 626–629 (2003).
8. S. W. Kim, T. Shimoyama, H. Hosono, Solvated electrons in high-temperature melts and glasses of the room-temperature stable electride $[Ca_{24}Al_{28}O_{64}]^{4+}\cdot 4e^-$. *Science* **333**, 71–74 (2011).
9. K. Lee, S. W. Kim, Y. Toda, S. Matsuishi, H. Hosono, Dicalcium nitride as a two-dimensional electride with an anionic electron layer. *Nature* **494**, 336–340 (2013).
10. M. Kitano, Y. Inoue, Y. Yamazaki, F. Hayashi, S. Kanbara, S. Matsuishi, T. Yokoyama, S.-W. Kim, M. Hara, H. Hosono, Ammonia synthesis using a stable electride as an electron donor and reversible hydrogen store. *Nat. Chem.* **4**, 934–940 (2012).
11. H. Buchammagari, Y. Toda, M. Hirano, H. Hosono, D. Takeuchi, K. Osakada, Room temperature-stable electride as a synthetic organic reagent: Application to pinacol coupling reaction in aqueous media. *Org. Lett.* **9**, 4287–4289 (2007).
12. Y. Toda, S. Matsuishi, K. Hayashi, K. Ueda, T. Kamiya, M. Hirano, H. Hosono, Field emission of electron anions clathrated in subnanometer-sized cages in $[Ca_{24}Al_{28}O_{64}]^{4+}(4e^-)$. *Adv. Mater.* **16**, 685–689 (2004).
13. K. P. Faseela, Y. J. Kim, S.-G. Kim, S. W. Kim, S. Baik, Dramatically enhanced stability of silver passivated dicalcium nitride electride: Ag-Ca_2N. *Chem. Mater.* **30**, 7803–7812 (2018).
14. Y. Toda, Y. Kubota, M. Hirano, H. Hirayama, H. Hosono, Surface of room-temperature-stable electride $[Ca_{24}Al_{28}O_{64}]^{4+}(e^-)_4$: Preparation and its characterization by atomic-resolution scanning tunneling microscopy. *ACS Nano* **5**, 1907–1914 (2011).
15. P. V. Sushko, A. L. Shluger, Y. Toda, M. Hirano, H. Hosono, Models of stoichiometric and oxygen-deficient surfaces of subnanoporous $12CaO\cdot 7Al_2O_3$. *Proc. R. Soc. A* **467**, 2066–2083 (2011).
16. Y. Lu, J. Li, T. Tada, Y. Toda, S. Ueda, T. Yokoyama, M. Kitano, H. Hosono, Water durable electride Y_5Si_3: Electronic structure and catalytic activity for ammonia synthesis. *J. Am. Chem. Soc.* **138**, 3970–3973 (2016).
17. J. Wu, Y. Gong, T. Inoshita, D. C. Fredrickson, J. Wang, Y. Lu, M. Kitano, H. Hosono, Tiered electron anions in multiple voids of LaScSi and their applications to ammonia synthesis. *Adv. Mater.* **29**, 1700924 (2017).
18. H. F. Franzen, J. Graham, The lower sulphides of hafnium at high temperature. *J. Inorg. Nucl. Chem.* **28**, 377–380 (1966).
19. G. S. Marek, S. I. Troyanov, V. I. Tsirel'nikov, Crystal structure and thermodynamic characteristics of monobromides of zirconium and hafnium. *Zh. Neorg. Khim.* **24**, 890–893 (1979).
20. Y. Zhang, H. Wang, Y. Wang, L. Zhang, Y. Ma, Computer-assisted inverse design of inorganic electrides. *Phys. Rev. X* **7**, 011017 (2017).
21. M. Hirayama, S. Matsuishi, H. Hosono, S. Murakami, Electrides as a new platform of topological materials. *Phys. Rev. X* **8**, 031067 (2018).
22. R. R. Chianelli, M. B. Dines, Low-temperature solution preparation of Group 4B, 5B and 6B transition-metal dichalcogenides. *Inorg. Chem.* **17**, 2758–2762 (1978).
23. X. Zhang, Z. Xiao, H. Lei, Y. Toda, S. Matsuishi, T. Kamiya, S. Ueda, H. Hosono, Two-dimensional transition-metal electride Y_2C. *Chem. Mater.* **26**, 6638–6643 (2014).
24. J. Park, K. Lee, S. Y. Lee, C. N. Nandadasa, S. Kim, K. H. Lee, Y. H. Lee, H. Hosono, S.-G. Kim, S. W. Kim, Strong localization of anionic electrons at interlayer for electrical and magnetic anisotropy in two-dimensional Y_2C electride. *J. Am. Chem. Soc.* **139**, 615–618 (2017).
25. V. Postils, M. Garcia-Borràs, M. Solà, J. M. Luis, E. Matito, On the existence and characterization of molecular electrides. *Chem. Commun.* **51**, 4865–4868 (2015).
26. R. D. Shannon, Revised effective ionic radii and systematic studies of interatomic distances in halides and chalcogenides. *Acta Crys. A* **32**, 751–767 (1976).

27. J. S. Oh, C.-J. Kang, Y. J. Kim, S. Sinn, M. Han, Y. J. Chang, B.-G. Park, S. W. Kim, B. I. Min, H.-D. Kim, T. W. Noh, Evidence for anionic excess electrons in a quasi-two-dimensional Ca_2N electride by angle-resolved photoemission spectroscopy. *J. Am. Chem. Soc.* **138**, 2496–2499 (2016).
28. T. V. Perevalov, V. A. Gritsenko, S. B. Erenburg, A. M. Badalyan, H. Wong, C. W. Kim, Atomic and electronic structure of amorphous and crystalline hafnium oxide: X-ray photoelectron spectroscopy and density functional calculations. *J. Appl. Phys.* **101**, 053704 (2007).
29. S. J. C. Brossia, *ASM Handbook, Volume 13B, Corrosion: Materials* (ASM International, 2007).
30. J. Xie, H. Zhang, S. Li, R. Wang, X. Sun, M. Zhou, J. Zhou, X. W. Lou, Y. Xie, Defect-rich MoS_2 ultrathin nanosheets with additional active edge sites for enhanced electrocatalytic hydrogen evolution. *Adv. Mater.* **25**, 5807–5813 (2013).
31. S. Harinipriya, M. V. Sangaranarayanan, Hydrogen evolution reaction on electrodes: Influence of work function, dipolar adsorption, and desolvation energies. *J. Phys. Chem. B* **106**, 8681–8688 (2002).
32. G. Kresse, J. Furthmüller, Efficient iterative schemes for *ab initio* total-energy calculations using a plane-wave basis set. *Phys. Rev. B* **54**, 11169–11186 (1996).
33. P. E. Blöchl, Projector augmented-wave method. *Phys. Rev. B* **50**, 17953–17979 (1994).
34. J. P. Perdew, K. Burke, M. Ernzerhof, Generalized gradient approximation made simple. *Phys. Rev. Lett.* **77**, 3865–3868 (1996).
35. B. Silvi, A. Savin, Classification of chemical bonds based on topological analysis of electron localization functions. *Nature* **371**, 683–686 (1994).
36. R. F. W. Bader, Atoms in molecules. *Acc. Chem. Res.* **18**, 9–15 (1985).
37. H. B. Michaelson, The work function of the elements and its periodicity. *J. Appl. Phys.* **48**, 4729–4733 (1977).
38. J. F. S. Moulder, W. F. Sobol, P. E. Sobol, K. D. Bomben, *Handbook of X-Ray Photoelectron Spectroscopy* (Physical Electronics Inc., 1995).
39. C. C. Ahn, O. L. Krivanek, R. P. Burgner, M. M. Disko, P. R. Swann, *EELS Atlas: A Reference Collection of Electron Energy Loss Spectra Covering All Stable Elements*, (Gatan Inc., 1983).
40. P. Ewels, T. Sikora, V. Serin, C. P. Ewels, L. Lajaunie, A complete overhaul of the electron energy-loss spectroscopy and X-ray absorption spectroscopy database: eelsdb.eu. *Microsc. Microanal.* **22**, 717–724 (2016).

Acknowledgments

Funding: This work was supported by a National Research Foundation of Korea (NRF) grant funded by the Korean government (Ministry of Science & ICT) (no. 2015M3D1A1070639) and supported by the Institute for Basic Science (IBS-R011-D1). **Author contributions:** S.W.K. conceived the idea and organized the research. C.N.N., S.-G.K., J.B., K.L., Y.M., and S.W.K. carried out the computational studies. S.H.K. fabricated polycrystals and grew the single crystals. S.H.K. performed the XRD, XPS/UPS, and electrical transport measurements. S.H.K., K.H.L., K.L., S.-G.K., and S.W.K. analyzed the structural, electrical, and electronic properties. S.H.K., G.H., S.L., and Y.-M.K. carried out TEM experiments. S.H.K., S.L., S.H.O., Y.-M.K., and S.W.K. analyzed the TEM results. S.H.K. and K.C. performed electrochemical experiments and analyzed the data. All authors discussed the results and contributed to writing the manuscript. **Competing interests:** The authors declare that they have no competing interests. **Data and materials availability:** All data needed to evaluate the conclusions in the paper are present in the paper and/or the Supplementary Materials. Additional data related to this paper may be requested from the authors.

Submitted 31 December 2019
Accepted 9 April 2020
Published 5 June 2020
10.1126/sciadv.aba7416

Citation: S. H. Kang, J. Bang, K. Chung, C. N. Nandadasa, G. Han, S. Lee, K. H. Lee, K. Lee, Y. Ma, S. H. Oh, S.-G. Kim, Y.-M. Kim, S. W. Kim, Water- and acid-stable self-passivated dihafnium sulfide electride and its persistent electrocatalytic reaction. *Sci. Adv.* **6**, eaba7416 (2020).